Chemical Science

ROYAL SOCIETY OF CHEMISTRY

EDGE ARTICLE

View Article Online
View Journal | View Issue

Cite this: *Chem. Sci.*, 2021, **12**, 11213

All publication charges for this article have been paid for by the Royal Society of Chemistry

Received 21st May 2021
Accepted 20th July 2021

DOI: 10.1039/d1sc02772g

rsc.li/chemical-science

Plasmon-enabled N_2 photofixation on partially reduced Ti_3C_2 MXene†

Binbin Chang,[a] Yanzhen Guo,[c] Donghai Wu,[c] Li Li, *[a] Baocheng Yang*[c] and Jianfang Wang *[b]

Benefiting from the superior conductivity, rich surface chemistry and tunable bandgap, Ti_3C_2 MXene has become a frontier cocatalyst material for boosting the efficiency of semiconductor photocatalysts. It has been theoretically predicted to be an ideal material for N_2 fixation. However, the realization of N_2 photofixation with Ti_3C_2 as a host photocatalyst has so far remained experimentally challenging. Herein, we report on a sandwich-like plasmon- and an MXene-based photocatalyst made of Au nanospheres and layered Ti_3C_2, and demonstrate its efficient N_2 photofixation in pure water under ambient conditions. The abundant low-valence Ti ($Ti^{(4-x)+}$) sites in partially reduced Ti_3C_2 (r-Ti_3C_2) produced by surface engineering through H_2 thermal reduction effectively capture and activate N_2, while Au nanospheres offer plasmonic hot electrons to reduce the activated N_2 into NH_3. The $Ti^{(4-x)+}$ active sites and plasmon-generated hot electrons work in tandem to endow r-Ti_3C_2/Au with remarkably enhanced N_2 photofixation activity. Importantly, r-Ti_3C_2/Au exhibits ultrahigh selectivity without the occurrence of competing H_2 evolution. This work opens up a promising route for the rational design of efficient MXene-based photocatalysts.

Introduction

Nitrogen is a requisite nutrient for all organisms on the Earth. Although N_2 occupies ~78 vol% of the atmosphere, its efficient utilization by organisms is greatly hindered because of the strong N≡N bond (945 kJ mol^{-1}).[1,2] Atmospheric N_2 is continuously fixed into biologically usable forms of nitrogen, such as NH_3 and NO_3^-. At the same time, the fixed forms of nitrogen are also continuously converted back to N_2 in nature, constituting a giant nitrogen cycle (Fig. S1†).[3] In this cycle, synthesized NH_3 not only is used as an indispensable chemical feedstock but also can act as a potential hydrogen carrier owing to its high hydrogen density (17.6 wt%) and low liquefying pressure (~8 atm).[4,5] In addition, the obtained H_2 and O_2 can be utilized in fuel cells. As a result, the realization of such a nitrogen cycle will be meaningful in developing sustainable clean energy and relieving environmental pollution. The NH_3 synthesis is a critical step in the cycle. Traditionally, NH_3 is produced through the industrial Haber–Bosch process. However, this process requires high temperatures (>300 °C) and high pressures (>100 atm) with a massive energy consumption and a huge amount of CO_2 emission.[6,7] Because of the energy input and carbon footprint, it is highly desired to explore a promising artificial nitrogen fixation strategy under benign conditions for a sustainable, green and safe NH_3 production.

Nitrogen photofixation offers an approach for achieving the energy-saving and environmentally friendly NH_3 synthesis under ambient conditions with renewable solar energy as the driving force.[8–10] In N_2 photofixation, H_2 is replaced by H_2O as a reducing agent. N_2 and $3H_2O$ are converted to $2NH_3$ and $1.5O_2$.[11–17] The key is to design an efficient photocatalyst. Two-dimensional (2D) photocatalysts exhibit unique merits in solar-to-chemical energy conversion.[18–22] MXenes, a family of 2D layered transition metal carbides, nitrides or carbonitrides, have aroused much interest since the first report in 2011.[23] Benefiting from the metallic conductivity, abundant surface terminal groups, large surface-to-volume ratio, excellent hydrophilic and ion transport properties, MXenes have been explored in diverse fields.[24–26] Ti_3C_2, the first reported MXene, possesses several unique characteristics.[24,25] (i) Its high conductivity enables excellent charge transfer kinetics, favoring the rapid migration and efficient separation of photogenerated electrons and holes; (ii) abundant exposed metal sites offer many active sites for catalysis; (iii) adjustable terminal groups (OH, O, F, *etc.*) bring a tunable bandgap and optical absorption, enabling facile regulation of the photocatalytic performance;

[a]*Shanghai Key Laboratory of Green Chemistry and Chemical Processes, School of Chemistry and Molecular Engineering, East China Normal University, Shanghai 200241, China. E-mail: lli@chem.ecnu.edu.cn*

[b]*Department of Physics, The Chinese University of Hong Kong, Shatin, Hong Kong SAR, China. E-mail: jfwang@phy.cuhk.edu.hk*

[c]*Henan Provincial Key Laboratory of Nanocomposites and Applications, Institute of Nanostructured Functional Materials, Huanghe Science and Technology College, Zhengzhou 450006, China. E-mail: baochengyang@infm.hhstu.edu.cn*

† Electronic supplementary information (ESI) available. See DOI: 10.1039/d1sc02772g

(iv) excellent surface hydrophilicity improves the interfacial connection with other materials, facilitating the formation of heterostructures. Ti_3C_2 has therefore become a research hotspot in photocatalysis.[27–30] Theoretical calculations have shown that Ti_3C_2 presents valid N_2-philicity and the ability to chemisorb and activate N_2, suggesting that Ti_3C_2 can be a promising material for N_2 capture and reduction.[31] Unfortunately, the extremely low Fermi level and metallic nature of Ti_3C_2 make it a superior electron acceptor, resulting in a poor separation efficiency of photogenerated electrons and holes.[32,33] In addition, the narrow bandgap of Ti_3C_2 makes N_2 photoreduction difficult.[34] As a result, it has remained challenging to realize N_2 photofixation solely with Ti_3C_2.

Plasmonic metal nanoparticles possess extraordinary optical properties that arise from localized surface plasmon resonance (LSPR) and offer a powerful means for boosting the photocatalytic activity.[18,35] LSPR-enhanced photocatalysis mainly relies on the extension of light absorption to the long-wavelength range and the enhancement of the local electric field. Plasmonic hot electrons can drive reduction reactions and improve photocatalytic NH_3 synthesis.[18,36–38] The plasmon-intensified electric field can promote the photogeneration of charge carriers in semiconductors.[39,40] As a result, combining plasmonic metal nanoparticles with 2D MXenes is expected to be a feasible strategy for constructing efficient photocatalysts for NH_3 production.

Herein, we report on the construction of a Au nanosphere-embedded, partially reduced, and layered Ti_3C_2 (r-Ti_3C_2) photocatalyst with a unique sandwich-like architecture for efficient N_2 photofixation under ambient conditions. r-Ti_3C_2 shows an expanded layer spacing and exposes many low-valence Ti sites ($Ti^{(4-x)+}$) on the edge and basal planes, which serve as active sites for N_2 activation. The unique sandwich-like, Au nanosphere-embedded r-Ti_3C_2 not only provides a large number of $Ti^{(4-x)+}$ active sites but also brings a high contact area between Au nanospheres and r-Ti_3C_2, improving the probability of excited charge carriers to interact with the reaction solution. Moreover, the embedding of Au nanospheres hinders the self-stacking of the r-Ti_3C_2 layers, benefiting the exposure of the active sites and boosting the effective utilization of the active sites and charge carriers. The hot electrons photoexcited on the plasmonic Au nanospheres inject into r-Ti_3C_2 and thereby reduce $Ti^{(4-x)+}$ site-activated N_2 into NH_3. The charge carrier recombination is largely suppressed because the electrons and holes are located in r-Ti_3C_2 and the Au nanospheres, respectively. The photocatalysts exhibit a superior activity for N_2 photofixation in pure water at ambient temperature and pressure. Our strategy opens up new opportunities for designing MXene/(plasmonic metal) nanostructures to achieve efficient photo-driven N_2 fixation.

Results and discussion

Materials synthesis and characterization

The Au nanosphere-embedded, partially reduced, and layered Ti_3C_2 with a unique sandwich-like architecture was prepared by a solvent-driven approach (Fig. 1a; see Experimental in the ESI†). First, the Al layers in layered Ti_3AlC_2 particles (Fig. S2†) were etched by HF to produce layered Ti_3C_2 with abundant O, OH and F terminations. During etching, some carbon atoms were replaced by oxygen atoms in the lattice of Ti_3C_2.[41] Second, Ti_3C_2 was then thermally treated in a N_2/H_2 atmosphere to alter its surface chemistry and generate oxygen vacancies (OVs) through H_2 reduction. Third, the Au nanospheres were driven by H_2O and gradually interlaminated in layered r-Ti_3C_2, resulting in a unique sandwich-like structure.

Scanning electron microscopy (SEM) imaging (Fig. 1b) reveals the accordion-like multilayered structure of Ti_3C_2, suggesting the successful etching of the Al layers. The layered texture is well kept in r-Ti_3C_2 (Fig. 1c), indicating that the H_2 treatment does not deteriorate the original layered structure. The Au nanospheres dispersed in aqueous solutions exhibit an extinction peak at 518 nm (Fig. S3†). Their sizes are uniform (Fig. 1d), as revealed by transmission electron microscopy (TEM), with an average diameter of 12.8 ± 0.7 nm (Fig. S4†). In the low-magnification SEM images of Ti_3C_2/Au and r-Ti_3C_2/Au (Fig. S5†), a unique sandwich-like architecture is clearly observed. The Au nanospheres are interlaminated between the MXene layers and uniformly distributed on the basal planes. High-magnification SEM imaging further shows clearly that the Au nanospheres are uniformly interlaminated in the MXene layers (Fig. 1e and f). The X-ray diffraction (XRD) of Ti_3AlC_2 (Fig. S6a†) reveals a strong and typical diffraction pattern of the pure Ti_3AlC_2 phase (JCPDS no. 52-0875). After HF treatment, the strong (002) peak exhibits a downshift from 9.55° to 9.05°, which corresponds to a *c*-lattice parameter (*c*-LP) increase from 18.53 Å to 19.48 Å, implying an interlayer spacing of 0.98 nm in Ti_3C_2. In addition, the disappearance of the intense peak at $2\theta = 39.08°$ in Ti_3AlC_2 after HF etching verifies the removal of the Al layers.[42] Taken together, these results confirm the successful synthesis of Ti_3C_2 MXene. After H_2 reduction, r-Ti_3C_2 displays a similar XRD pattern to Ti_3C_2 (Fig. 1g), except an additional (006) diffraction peak at $2\theta = 28.5°$ (Fig. S6b†), reflecting a better-organized multilayered structure with more opened Ti_3C_2 layers.[43] The XRD patterns also reveal the coexistence of the cubic Au phase (JCPDS no. 01-1172) and Ti_3C_2 in Ti_3C_2/Au and r-Ti_3C_2/Au (Fig. 1g). Compared to Ti_3C_2, the (002) peak shows clear and different shifts among r-Ti_3C_2, Ti_3C_2/Au and r-Ti_3C_2/Au (Fig. 1h). A slight shift of the (002) peak to a higher angle of 9.12° for r-Ti_3C_2 corresponds to a *c*-LP decrease from 19.48 Å to 19.25 Å, signifying a reduced interlayer spacing of 0.96 nm in r-Ti_3C_2. The small *c*-LP change of r-Ti_3C_2 can be ascribed to the elimination of H_2O molecules interlaminated between the Ti_3C_2 layers or surface reactions during H_2 reduction.[23,44] The (002) peak shifts down to $2\theta = 8.95°$ for sandwich-like Ti_3C_2/Au and r-Ti_3C_2/Au, which corresponds to a *c*-LP of 19.68 Å, indicative of an enlarged interlayer spacing of 1.00 nm. The increased interlayer spacing is probably caused by the intercalation of the Au nanospheres between the Ti_3C_2 and r-Ti_3C_2 segments.[45] Each segment contains multiple Ti_3C_2 layers, but its overall thickness is greatly reduced in comparison with the sample before the intercalation of the Au nanospheres. In the Raman spectra of Ti_3AlC_2 (Fig. S7†), four major peaks appearing at

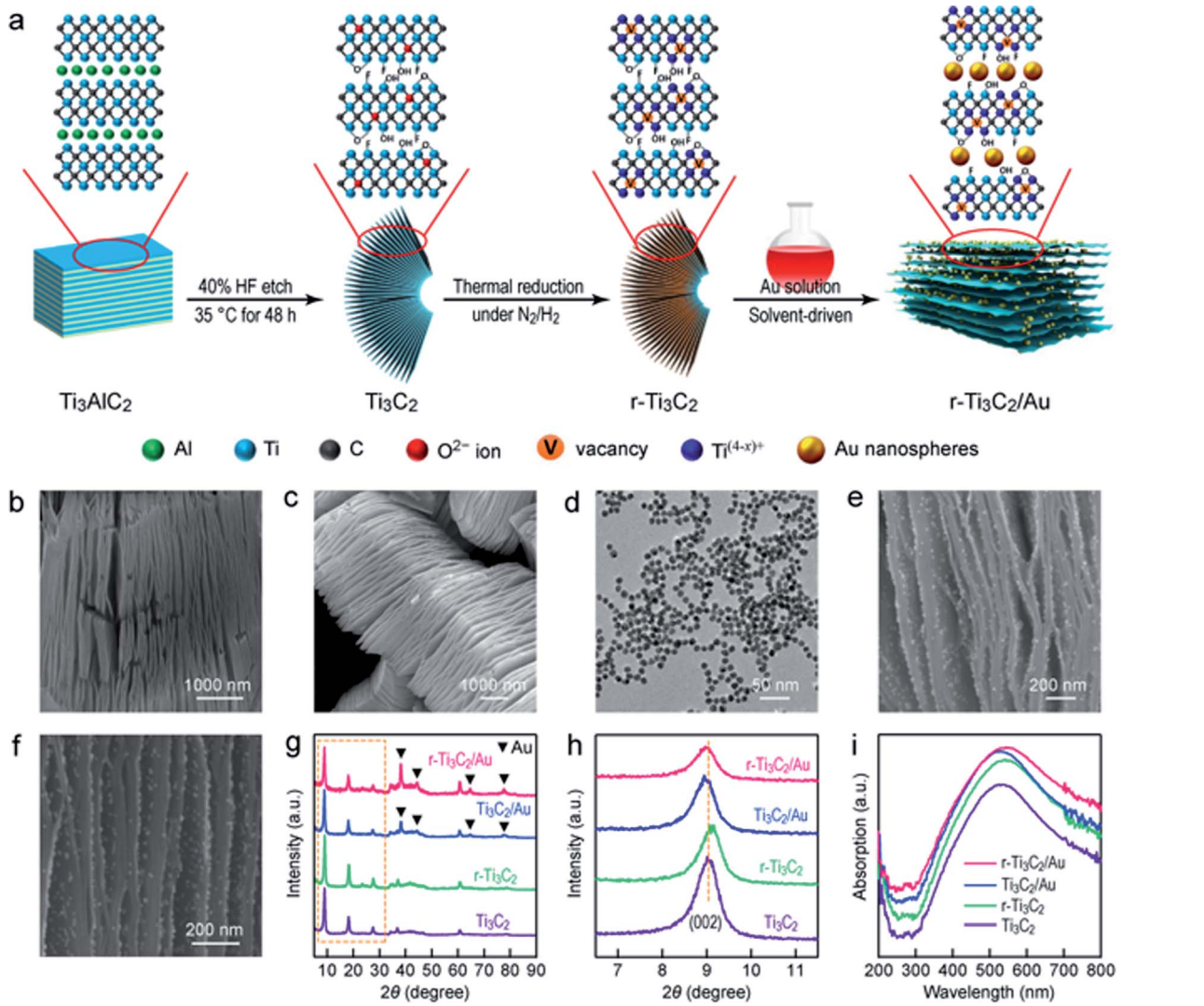

Fig. 1 Synthesis of the sandwich-like r-Ti_3C_2/Au nanostructure. (a) Schematic illustrating the synthesis process. The Ti_3C_2 layer and Au nanosphere components are not drawn on the same size scale. (b) SEM image of Ti_3C_2. (c) SEM image of r-Ti_3C_2. (d) TEM image of the Au nanospheres. (e) SEM image of Ti_3C_2/Au. (f) SEM image of r-Ti_3C_2/Au. (g) XRD patterns of Ti_3C_2, r-Ti_3C_2, Ti_3C_2/Au and r-Ti_3C_2/Au. (h) XRD peaks of Ti_3C_2, r-Ti_3C_2, Ti_3C_2/Au and r-Ti_3C_2/Au for the (002) lattice planes. (i) Absorption spectra of Ti_3C_2, r-Ti_3C_2, Ti_3C_2/Au and r-Ti_3C_2/Au.

145, 260, 410 and 605 cm^{-1} are the characteristic Raman bands of Ti_3AlC_2. They arise from the ω_1, ω_2, ω_3 and ω_4 Raman-active vibrational modes.[46,47] Ti_3C_2 and r-Ti_3C_2 show similar Raman peaks, with a highly intensified peak at 153 cm^{-1}, along with three weak peaks at 260, 428 and 610 cm^{-1}. All the four peaks can be ascribed to the Raman-active vibrational modes of Ti–C,[48,49] suggesting the successful etching of the Al atoms and the preservation of the Ti_3C_2 layers. In addition, two broad bands observed at 1350 and 1610 cm^{-1} for Ti_3C_2 and r-Ti_3C_2 correspond to the D- and G-bands of carbon, manifesting the existence of disordered carbon and ordered graphitic carbon, respectively. The larger peak intensities of the D- and G-bands in r-Ti_3C_2 reveal the existence of more disordered carbon after H_2 reduction, suggesting the formation of more oxygen defects in the carbon layers of r-Ti_3C_2.[50] Such oxygen defects can bring more active sites for N_2 adsorption on the surface of r-Ti_3C_2.

Ti_3C_2 shows clear absorption in the spectral region of 300–800 nm with a maximum at ~520 nm (Fig. 1i). r-Ti_3C_2 also exhibits a broad absorption band in the region of 300–800 nm, but the absorption maximum exhibits a slight redshift. This phenomenon is probably caused by the changes in the surface chemistry and terminal groups of r-Ti_3C_2, resulting in a changed bandgap.[51] Despite the broad light absorption, very few charge carriers can be photogenerated and separated in Ti_3C_2 and r-Ti_3C_2.[32–34] On the other hand, the efficient photothermal conversion of Ti_3C_2 MXene can facilitate surface catalytic reactions through the conversion of light to heat to activate the supported catalyst.[52] Unlike common plasmonic Au/semiconductor hybrid photocatalysts,[36,53] the absorption peak from the LSPR band of the Au nanospheres cannot be clearly observed in Ti_3C_2/Au or r-Ti_3C_2/Au. This result is likely caused by the spectral overlap between the LSPR of the Au nanospheres and the strong broad absorption of Ti_3C_2 MXene, which is

reflected by the enhanced absorption in the region of 500–600 nm. The charge transport ability is another key factor in photocatalysis. Electrochemical impedance spectroscopy (EIS) measurements were conducted under white light illumination in a N_2 atmosphere (Fig. S8†). A smaller semicircle in the obtained Nyquist plot implies a better charge transfer capability at the electrode–electrolyte interface. r-Ti_3C_2/Au exhibits the smallest arc radius, signifying a good charge transfer ability. The improved charge transfer ability can be attributed to the effective interfacial charge transfer in the sandwich-like r-Ti_3C_2/Au. Though the metallic Ti_3C_2 is difficult to photogenerate charge carriers, it can serve as an electron acceptor to capture the hot electrons generated by the plasmonic Au nanospheres owing to its superior electrical conductivity.[32]

Nitrogen photofixation

The photocatalytic N_2 fixation experiments were performed in N_2-saturated water under light illumination and ambient conditions in a quartz reactor (Fig. S9†). The produced ammonia amount was determined by Nessler's method, as shown by the calibration curve (Fig. S10†). Fig. 2a displays the time-dependent NH_4^+ concentrations over different photocatalysts under white light illumination. The Au nanospheres were found to be inactive for N_2 photofixation under both white and visible light. NH_4^+ was hardly detected over Ti_3C_2. The NH_4^+ concentration reached 10.7 and 18.3 μmol L^{-1} in 6 h over r-Ti_3C_2 and Ti_3C_2/Au, respectively. The N_2 photofixation activity of the r-Ti_3C_2/Au catalyst was greatly boosted to 216.8 μmol L^{-1} in 6 h. Under visible light (λ >400 nm), the produced NH_4^+ amounts of all catalysts decreased (Fig. 2b). The ammonia generation rates were normalized against the illumination time and the catalyst amount under both white and visible light (Fig. 2c). The NH_4^+ generation rate over r-Ti_3C_2/Au is 22.6 (12.4) μmol h^{-1} g_{cat}^{-1} under white light (visible light) illumination, which is 5.8 (5.9) and 10.2 (10.3) times those of Ti_3C_2/Au and r-Ti_3C_2, respectively.

To verify the nitrogen and proton sources of the produced NH_3, control experiments were carried out with r-Ti_3C_2/Au (Fig. S11†). NH_4^+ was not detected when N_2 or H_2O was replaced with Ar or aprotic acetonitrile, suggesting that the nitrogen and proton sources for the NH_4^+ formation are from N_2 and H_2O, respectively. In addition, NH_4^+ cannot be generated in dark, suggesting that light is an essential driving force for N_2 photofixation. To further corroborate the origin of the produced NH_3, an isotope labeling experiment was performed using $^{14}N_2$ and $^{15}N_2$ as the nitrogen sources. The obtained $^{14}NH_4Cl$ and $^{15}NH_4Cl$ were measured by ^1H nuclear magnetic resonance (NMR) spectroscopy (Fig. 3a). The triplet and doublet peaks corresponding to $^{14}NH_4^+$ and $^{15}NH_4^+$ can be clearly observed in the ^1H NMR spectra of the photocatalytic reaction solutions when $^{14}N_2$ and $^{15}N_2$ were used as the feed gas, respectively. This result verifies that the produced NH_4^+ indeed originated from N_2 photofixation. Moreover, the evolution of O_2 was also detected during the N_2 photofixation process in a sealed reactor (Fig. S12a†). To assess whether O_2 was produced during the N_2 photofixation reaction catalyzed by r-Ti_3C_2/Au, the reactor was evacuated, bubbled with N_2, and then sealed. Upon illumination for 1 h under white light, O_2 was detected. The generated O_2 should result from the oxidization of H_2O by the hot holes in the Au nanospheres.[54] Its amount is about three fourths that of NH_4^+ (Fig. S12b†), close to the stoichiometric ratio of 3 : 4 according to the reaction $N_2 + 3H_2O \rightarrow 2NH_3 + 1.5O_2$, proving that NH_3 is generated by coupling the activated N_2 with the protons from H_2O. Importantly, H_2 was not detected during the

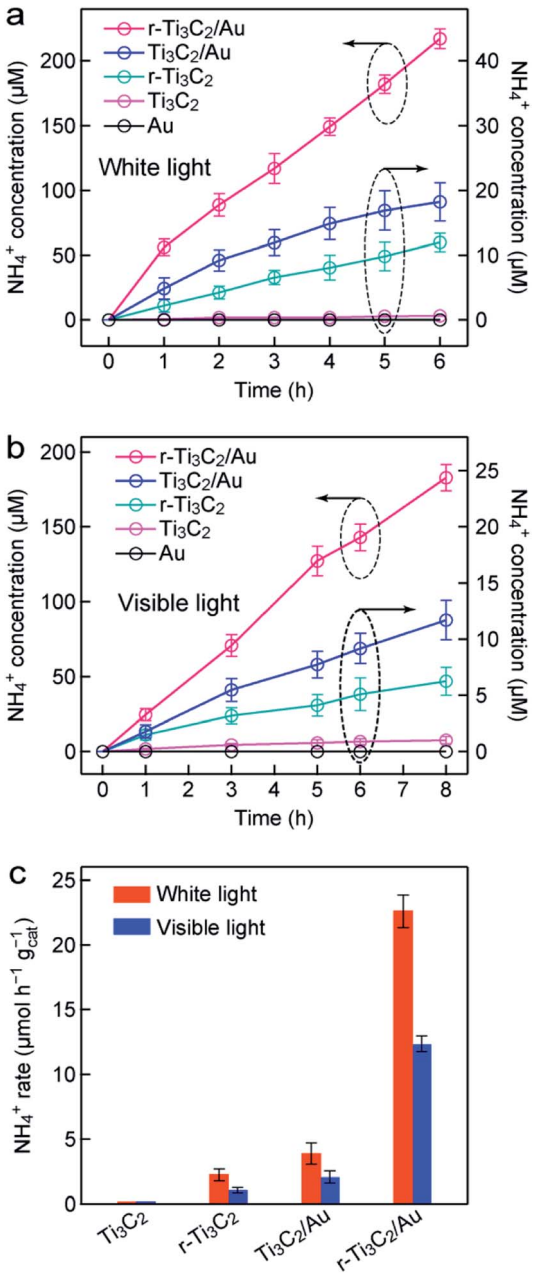

Fig. 2 N_2 photofixation over Au, Ti_3C_2, r-Ti_3C_2, Ti_3C_2/Au, and r-Ti_3C_2/Au. (a) Time courses of the ammonia concentrations measured under white light illumination. (b) Time courses of the ammonia concentrations measured under visible light illumination (λ >420 nm). (c) Ammonia production rates under white light and visible light. The rates for the Au nanospheres are not drawn because the Au nanospheres exhibit no activity for N_2 photofixation.

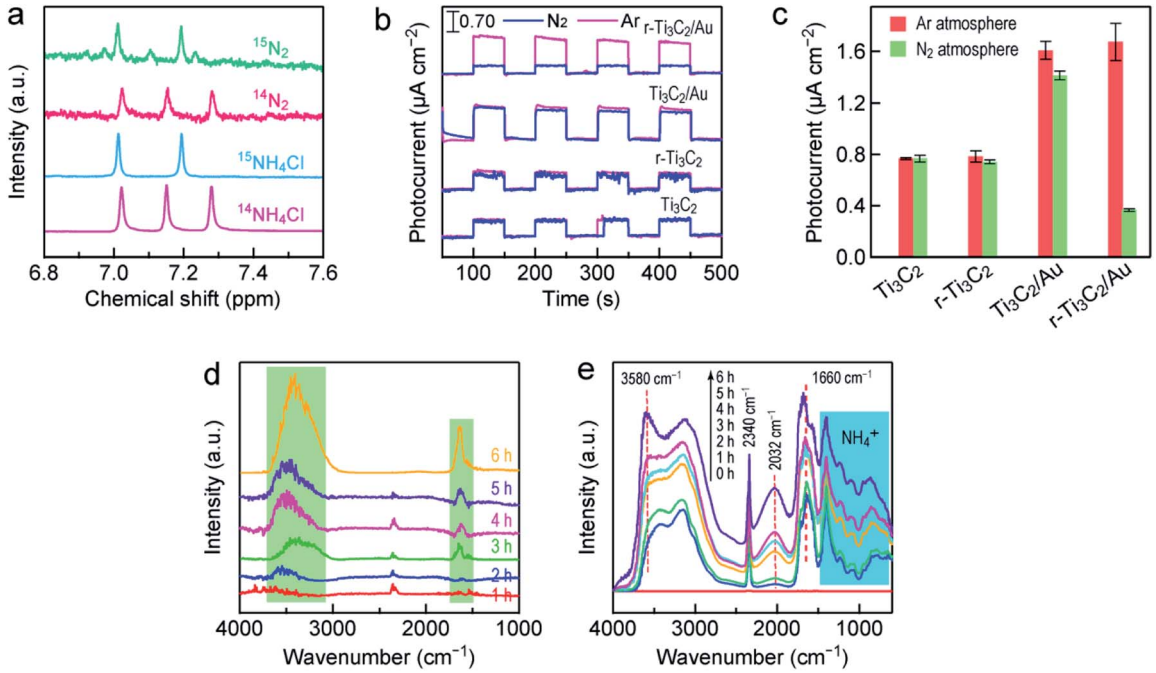

Fig. 3 Understanding the photocatalytic N_2 fixation process. (a) ^{1}H NMR spectra of the solutions after the N_2 fixation reaction over r-Ti_3C_2/Au in $^{15}N_2$ and $^{14}N_2$ atmospheres. The bottom two spectra were taken from the standard $^{15}NH_4Cl$ and $^{14}NH_4Cl$ solutions. (b) Photocurrent responses of the different catalysts recorded in Ar and N_2 atmospheres, with the white light illumination switched on and off repeatedly. (c) Photocurrent densities of the different catalysts in Ar and N_2 atmospheres under white light illumination. (d) *In situ* DRIFT spectra recorded as a function of time during the N_2 photofixation reaction over r-Ti_3C_2/Au in the Ar atmosphere. (e) *In situ* DRIFT spectra recorded as a function of time during the N_2 photofixation reaction over r-Ti_3C_2/Au in the N_2 atmosphere.

N_2 photofixation process (Fig. S12a†), suggesting the absence of the competing hydrogen evolution reaction. r-Ti_3C_2/Au is therefore a highly selective photocatalyst for N_2 fixation.

To reveal the mechanism of the photocatalytic N_2 fixation, photocurrent tests were first performed under white light illumination in both N_2 and Ar atmospheres (Fig. 3b). For Ti_3C_2, the photocurrent densities measured in Ar and N_2 are nearly the same and reach ~0.76 μA cm^{-2} (Fig. 3c). The photocurrent density of r-Ti_3C_2 is similar to that of Ti_3C_2, and the photocurrent in N_2 shows a slight reduction. In the presence of the Au nanospheres, the photocurrents of Ti_3C_2/Au and r-Ti_3C_2/Au are enhanced in Ar because of the LSPR effect, and both reach ~1.65 μA cm^{-2}. There is a small decrease of ~0.15 μA cm^{-2} in the photocurrent density of Ti_3C_2/Au when the Ar atmosphere changed to N_2, which means a slight electron consumption for the reduction of N_2 molecules. Remarkably, the photocurrent density of r-Ti_3C_2/Au in N_2 is only one fifth of that in Ar, suggesting that the four fifth difference in photocurrent is consumed to reduce N_2 molecules. As a result, r-Ti_3C_2/Au displays a remarkable N_2 photofixation activity (Fig. 2). To look into the reaction process of adsorbed H_2O and N_2 and prove the activation and reduction of N_2 on the surface of r-Ti_3C_2/Au, *in situ* diffuse-reflectance infrared Fourier transform spectroscopy (DRIFTS) was employed to monitor the N_2 photofixation process. To record the DRIFT spectra, r-Ti_3C_2/Au was exposed to water vapor-saturated N_2 under white light illumination, which allows for the investigation of the time-dependent change of the molecular species adsorbed on the catalyst. In the control experiment performed in an Ar atmosphere, two clear absorption peaks at 1660 and 3580 cm^{-1}, corresponding to the characteristic bending modes of adsorbed H_2O molecules,[36] were observed. Their intensities were enhanced as the reaction time was prolonged (Fig. 3d). No absorption bands related to the N-containing species were detected, which further indicates that the nitrogen in NH_3 truly originated from N_2 molecules. The time-dependent DRIFT spectra recorded after the injection of N_2 under white light reveal that several absorption peaks gradually appear as the illumination time was prolonged from 0 to 6 h. The signal at 2340 cm^{-1} can be ascribed to strongly chemisorbed N_2 molecules.[55] The absorption band at 2032 cm^{-1} is believed to arise from the Ti–N=N complex formed through N_2 binding to the Ti^{3+} sites.[56] The absorption band at ~3160 cm^{-1} corresponds to the adsorbed ammonia.[9,37] Furthermore, the characteristic absorption band at 1410 cm^{-1} assigned to the NH_4^+ deformation vibration is intensified with increasing illumination time.[37,57] These DRIFTS results provide strong evidence that N_2 molecules can be adsorbed, activated and further reduced to form NH_4^+ under light illumination.

To further understand the photocatalytic N_2 fixation performance of r-Ti_3C_2/Au, the effect of the Au nanosphere amount in r-Ti_3C_2/Au was systematically investigated. The amount of embedded Au nanospheres was determined by inductively coupled plasma mass spectrometry (ICP-MS; Fig. S13†). Fig. 4a shows the high-magnification SEM images of the Au/r-Ti_3C_2 samples that were embedded with the 12.8 nm-sized Au nanospheres at 0.49, 1.11, 1.78 and 2.28 wt% relative to the total

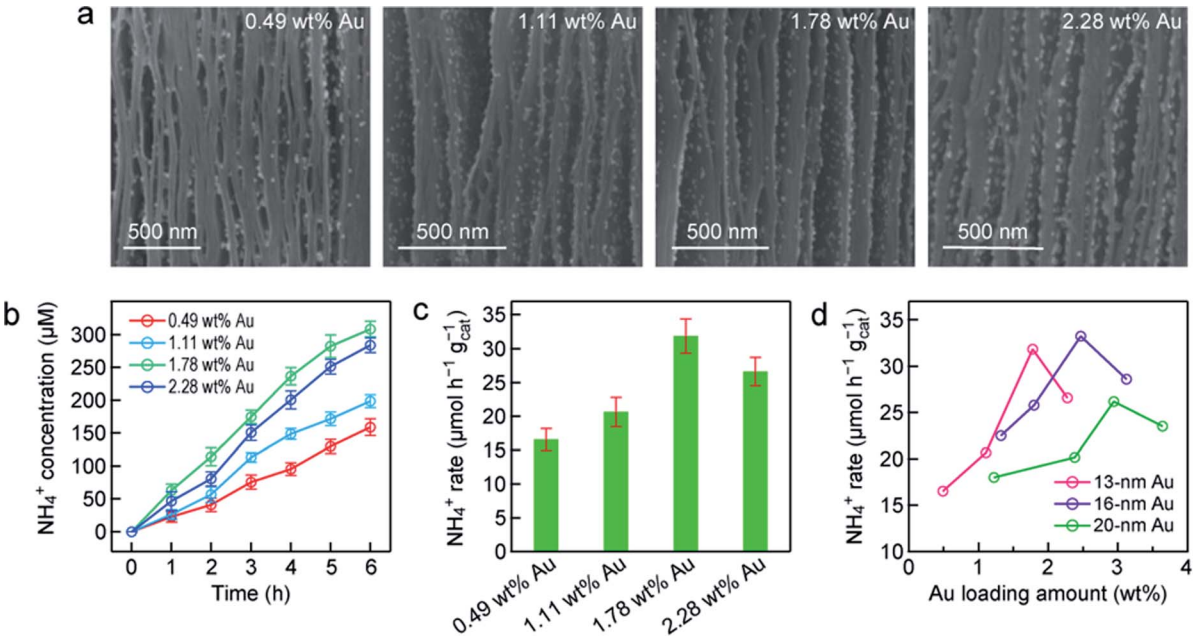

Fig. 4 Nitrogen photofixation over different r-Ti_3C_2/Au samples. (a) SEM images of r-Ti_3C_2/Au containing the 13 nm-sized Au nanospheres at different amounts indicated in the images. (b) Time courses of the ammonia concentrations measured under white light for the samples shown in (a). (c) Ammonia production rates under white light for the samples shown in (a). (d) Photocatalytic ammonia production rates as a function of the loaded Au amount for r-Ti_3C_2/Au containing the differently sized Au nanospheres.

amount of Au and r-Ti_3C_2, respectively. The unique sandwich-like architecture is observable for all samples. The Au nanospheres are uniformly distributed on the basal planes even when the loaded Au amount is increased to 1.78 wt%. As the embedded Au amount is increased to 2.28 wt%, aggregation occurs. The NH_4^+ concentrations catalyzed by the Au/r-Ti_3C_2 samples with different Au amounts increase with the illumination time under white light (Fig. 4b). When the embedded Au amount is increased from 0.49 to 1.78 wt%, the produced NH_4^+ amount steadily increases within the same reaction time. The r-Ti_3C_2/Au sample with the Au amount of 1.78 wt% gives the highest amount of the produced NH_4^+, whose concentration reaches 307.8 μmol L^{-1} in 6 h. However, when the embedded Au amount is further increased to 2.28 wt%, the generated NH_4^+ concentration is clearly reduced. Similarly, the normalized NH_4^+ production rate first increases with the Au amount, reaches the highest value of 31.8 μmol h^{-1} g_{cat}^{-1} at the loaded Au amount of 1.78 wt%, and then decreases (Fig. 4c). To further explore the relationship between the N_2 photofixation activity and the LSPR effect of the Au nanospheres, r-Ti_3C_2/Au with different Au nanosphere sizes and amounts were prepared. The uniform Au nanospheres with average sizes of 16.1 ± 0.8 (Fig. S14†) and 21.0 ± 0.8 nm (Fig. S15†) were synthesized. The unique sandwich-like structure with the uniform distribution of the Au nanospheres in the interlayers was obtained. Similarly, a high Au amount results in a reduction in the NH_4^+ production. Fig. 4d summarizes the relationship between the NH_4^+ generation rate and the loaded Au nanosphere size and amount. For the same Au size, the NH_4^+ production rates show a nearly volcano-shaped dependence on the embedded Au amount. An optimal N_2 photofixation performance is achieved at a particular Au amount, which increases with the Au nanosphere diameter. The optimal Au amount for each size can be attributed to the enhanced LSPR effect with increasing amounts of Au nanospheres. The decrease in the N_2 photofixation rate at a higher Au amount should be caused by the aggregation of the Au nanospheres and/or the blocking of the active sites on r-Ti_3C_2 for N_2 adsorption by the excessive Au nanospheres. The N_2 photofixation rates for the r-Ti_3C_2/Au samples containing the 20 nm-sized Au nanospheres are generally smaller than those of the samples containing the 13 nm- and 16 nm-sized Au nanospheres. This is probably because the number of Au nanospheres plays a more important role than the absorption cross-section for the LSPR effect in N_2 photofixation. The optimal sample was found to be r-Ti_3C_2/Au containing the 16 nm-sized Au nanospheres at 2.45 wt%. This sample gives a NH_4^+ production rate of 33.8 μmol h^{-1} g_{cat}^{-1}.

Au nanospheres capped with different molecules were next employed to study their assembly with r-Ti_3C_2 and in turn their effect on N_2 photofixation. Au nanospheres coated with cetyltrimethylammonium bromide (CTAB) were chosen. They exhibit good dispersibility and uniform sizes with an average diameter of 19.8 ± 0.7 nm (Fig. S16†). The CTAB-capped Au nanospheres were found to predominantly assemble onto the edges of the r-Ti_3C_2 layers (Fig. 5a). The resultant sample is therefore denoted r-Ti_3C_2/edge-Au. The CTAB-capped Au nanospheres are positively charged with a zeta potential of +34.2 mV, and the layered r-Ti_3C_2 sample is negatively charged with a zeta potential of −28.8 mV (Fig. S17†). The two components can therefore spontaneously assemble together through electrostatic attraction during solvent evaporation. The assembly results in an intimate contact between the Au nanospheres and the edges of r-Ti_3C_2. It also implies that

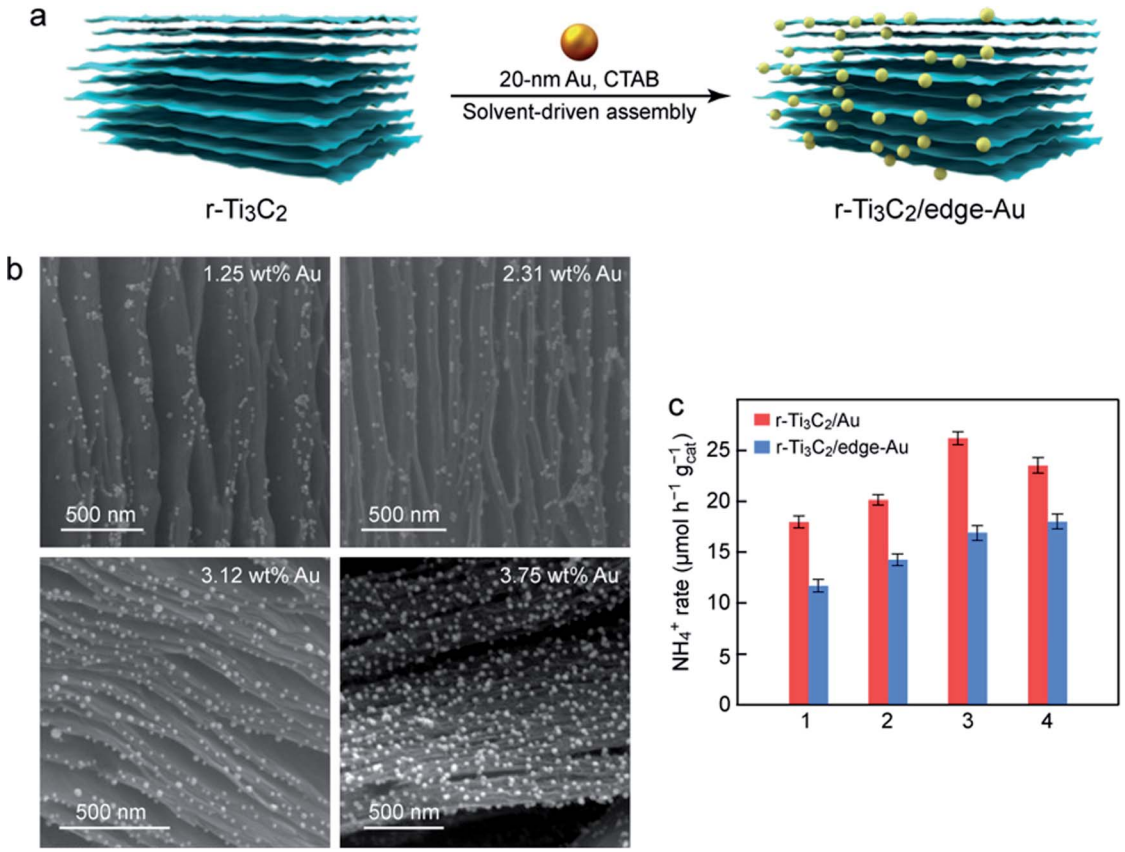

Fig. 5 Characterization and N_2 photofixation of r-Ti_3C_2/edge-Au. (a) Schematic illustrating the synthesis process of r-Ti_3C_2/edge-Au. (b) SEM images of r-Ti_3C_2/edge-Au with different loaded Au amounts. (c) Comparison of the ammonia production rates over the sandwich-like r-Ti_3C_2/Au and the r-Ti_3C_2/edge-Au catalysts under white light illumination. The sizes of the Au nanospheres in both catalysts are ~20 nm. The loaded Au amounts in both catalysts are nearly the same in each group from 1 to 4.

the electrostatic attraction force is stronger than the solvent-driven force. In contrast, the citrate-capped Au nanospheres cannot be adsorbed onto the edges of r-Ti_3C_2 due to electrostatic repulsion. They are driven into the interlayers of r-Ti_3C_2 by the solvent, producing the sandwich-like nanostructure. The SEM images (Fig. 5b) of r-Ti_3C_2/edge-Au reveal that the Au nanospheres are distributed along the edges of the layered r-Ti_3C_2 without clear aggregation, even when the Au amount is increased from 1.25 to 3.75 wt%. The N_2 photofixation activity of r-Ti_3C_2/edge-Au increases with increasing Au amounts (Fig. S18†). The photocatalytic N_2 fixation performances of r-Ti_3C_2/Au with the Au nanospheres located at different positions are compared under the identical nanosphere diameter of ~20 nm and the close amounts of Au (Fig. 5c). Considerable reductions in the NH_4^+ production rate are seen for the r-Ti_3C_2/edge-Au catalysts. The reductions are probably caused by the relatively large average distance from the edge-positioned Au nanospheres, which act as the electron sources, to the active sites on the layers of r-Ti_3C_2. The large distance increases the probability for electrons to get lost during their transport.

Active sites and N_2 photofixation mechanism

The active sites of Ti_3C_2 MXene are vital for N_2 adsorption and activation and crucial for the utilization of Ti_3C_2 MXene in N_2 photofixation. X-ray photoelectron spectroscopy (XPS) was performed on Ti_3C_2 and r-Ti_3C_2 to examine the active sites (Fig. 6a and b). The peak at 454.6 eV for Ti_3C_2 and r-Ti_3C_2 can be assigned to the Ti–C bond. The peak appearing at 458.5 eV for both samples can be assigned to TiO_{2-x}, which arises mainly from the Ti atoms surrounded by O^{2-} ions in the lattice owing to the replacement of some carbon atoms by oxygen atoms during etching.[37,50] The peaks at 455.3 (460.2), 456.1(461.2) and 457.1 eV (462.3 eV) come from $2p_{3/2}$ ($2p_{1/2}$) of Ti^{2+}, Ti^{3+} and Ti^{4+}, respectively. Compared to Ti_3C_2, r-Ti_3C_2 exhibits an enhanced fraction of Ti^{3+} with a diminished fraction of Ti^{4+} (Table S1†), manifesting the partial reduction of Ti^{4+} to the low-valence states of Ti^{3+} or Ti^{2+} through H_2 treatment. The low-valence state Ti^{3+} has been known to be active for N_2 chemisorption. No clear changes were observed in the Ti 2p peaks for Ti_3C_2/Au and r-Ti_3C_2/Au, suggesting that the embedding of the Au nanospheres does not change the chemical state of Ti. The O 1s spectra of Ti_3C_2 and r-Ti_3C_2 can be fitted with two peaks at 529.4 and 531.2 eV (Fig. S19a†), which are, respectively, derived from Ti–O and Ti–OH. The decreased intensity ratio between Ti–OH and Ti–O for r-Ti_3C_2 is attributed to the H_2 treatment. After the loading of the Au nanospheres, a new peak appears at ~532.3 eV (Fig. S19b†), suggesting the strong affinity between the Au nanospheres and the Ti_3C_2 layers through the formation of Au–O–Ti.[58] The peaks at 83.7 and 87.3 eV in Ti_3C_2/Au and r-Ti_3C_2/Au

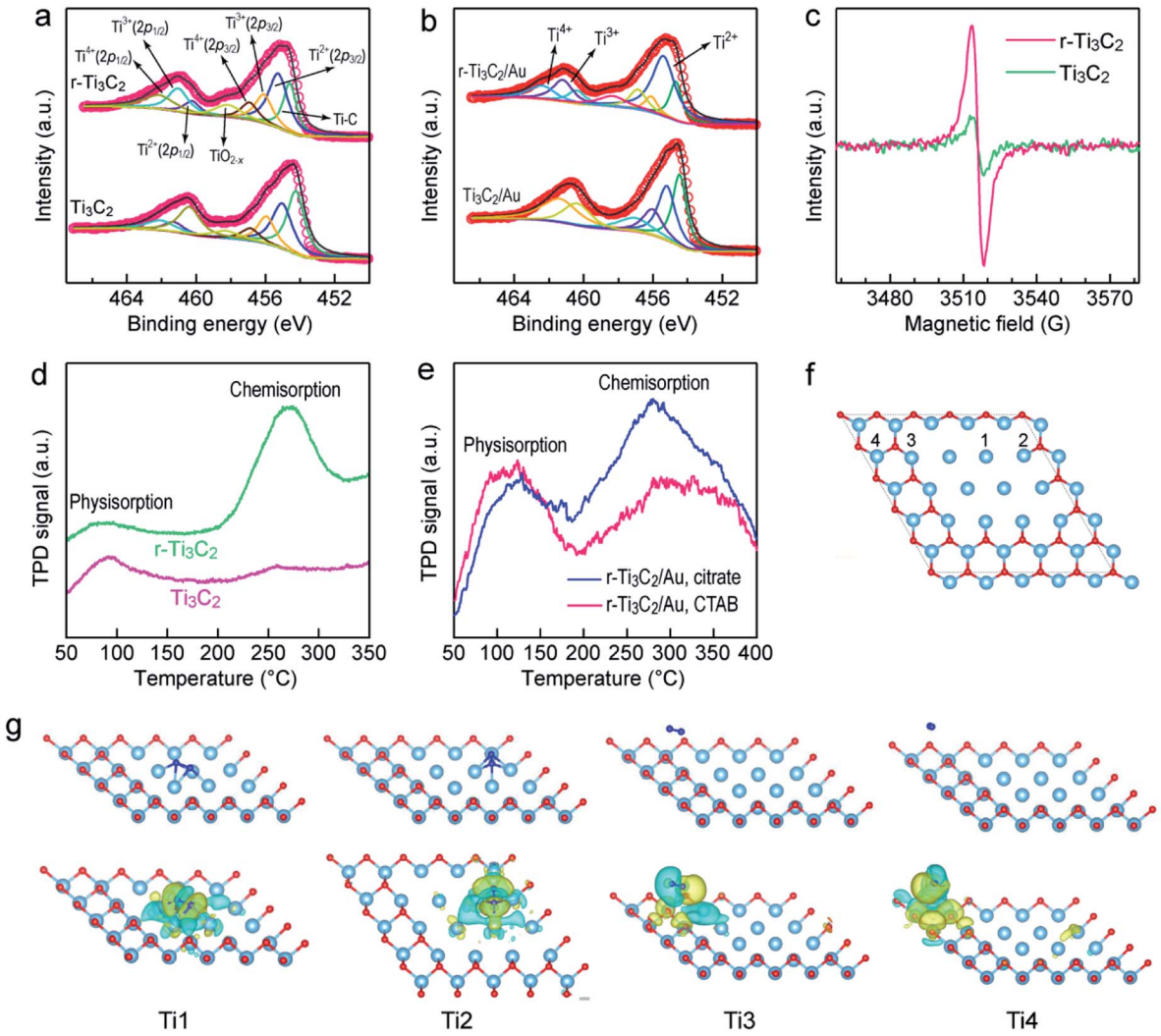

Fig. 6 Adsorption and activation of N_2 molecules. (a) Ti 2p XPS spectra of Ti_3C_2 and r-Ti_3C_2. (b) Ti 2p XPS spectra of Ti_3C_2/Au and r-Ti_3C_2/Au. (c) EPR spectra of Ti_3C_2 and r-Ti_3C_2. (d) N_2 TPD profiles of Ti_3C_2 and r-Ti_3C_2. (e) N_2 TPD profiles of r-Ti_3C_2/Au and r-Ti_3C_2/edge-Au. (f) Various Ti sites on r-Ti_3C_2. Only the top Ti layer terminated with a layer of O atoms is shown. (g) Adsorption configuration (top row) and charge density difference (bottom row) of a N_2 molecule adsorbed at different Ti sites on the r-Ti_3C_2 surface. Light blue balls: Ti; red balls: O; and dark blue balls: N. Yellow cloud: electron enrichment and cyan cloud: electron depletion.

(Fig. S19c†) arise, respectively, from Au $4f_{5/2}$ and Au $4f_{7/2}$, further verifying the successful assembly of the Au nanospheres onto the Ti_3C_2/r-Ti_3C_2 layers. Low-temperature electron paramagnetic resonance (EPR) spectra were measured to further confirm the existence of Ti^{3+} and surface OVs (Fig. 6c). The EPR spectrum of Ti_3C_2 shows a weak signal at $g = 1.998$, which originated from the delocalized electrons of the O^{2-} ions in the lattice.[11,59] In comparison, r-Ti_3C_2 displays a stronger EPR peak with $g = 2.004$, demonstrating the formation of OVs caused by the H_2 treatment and the existence of more Ti^{3+} in r-T_3C_2.[57] Both XPS and EPR therefore reveal that r-Ti_3C_2 possesses a number of Ti^{3+} species and OVs in its framework, which can act as active sites for N_2 chemisorption. N_2 temperature-programmed desorption (TPD) further revealed the N_2 adsorption ability of different samples. Only one peak at ~100 °C was detected for Ti_3C_2 (Fig. 6d), which is caused by N_2 physisorption. In addition to the physisorption peak, r-Ti_3C_2 presents a strong peak at a higher temperature of ~250–300 °C, which should have originated from the chemisorption of N_2 molecules.[60] These results indicate that N_2 chemisorption occurs at the Ti^{3+} sites on the r-Ti_3C_2 framework through the electron donation from the OV-induced Ti^{3+}, as further discussed below.

Density functional theory (DFT) calculations were performed to investigate the chemisorption and activation of N_2 molecules on different Ti sites of Ti_3C_2 MXene (Fig. 6f). Upon adsorption of a N_2 molecule on the Ti1 site, the optimized N_2 coordination configuration shows that the N_2 molecule is chemisorbed on a Ti–Ti tripolymer center through a dinuclear end-on coordination mode, in which one N atom binds with the Ti–Ti tripolymer and the other binds with the Ti–Ti dimer (Fig. 6g). When a N_2 molecule is adsorbed on the Ti2 site, the optimized coordination configuration is similar to that of N_2 coordinated to the Ti1 site, but the adjacent two Ti1 sites are combined to form a Ti1–Ti2 tripolymer and a Ti1–Ti2 dimer (Fig. 6g). The Ti3

and Ti4 sites cannot adsorb N_2 molecules (Fig. 6g), which is probably caused by the weak interaction due to the strongly electronegative nature of the surface O-terminal groups.[61] To disclose the electron transfer between r-Ti_3C_2 and the adsorbed N_2, the charge density difference was calculated (Fig. 6g, bottom row). A clear charge density difference is observed for the Ti1 and Ti2 sites, suggesting the occurrence of electron transfer from r-Ti_3C_2 to the N_2 molecule. The electron-enriched isosurface on the adsorbed N_2 molecule exhibits a π-orbital feature, indicating that the d-orbital electrons on the adjacent Ti atoms at the Ti1-site are transferred to the captured N_2 molecule. As electrons are injected into the N_2 molecule, the N≡N triple bond is considerably weakened with an elongated bond length. The triple bond lengths of the N_2 molecules adsorbed at the Ti1 and Ti2 sites, respectively, increased to 1.351 and 1.345 Å, much longer than the value of 1.114 Å for a free N_2 molecule (Fig. S20a and b†). In addition, a distinct reduction in the electron density between the two N atoms is also observed, implying that electrons are donated from the highest occupied σ-orbital of the N_2 molecule to the adjacent Ti sites. Such phenomena of electron donation from N_2 to the metal and back-donation from the metal to N_2 also happen in M (transition metal)–N_2 complexes and have been discovered for many metals.[1,62,63] The strong activation of N_2 molecules through electron back-donation from transition metals with available d-orbital electrons plays a crucial role in boosting the photocatalytic N_2 fixation activity of the r-Ti_3C_2 catalyst.

In order to better understand the N_2 chemisorption, we also performed DFT calculations to examine the adsorption energy (E_{ad}) of N_2 at different sites on r-Ti_3C_2 MXene (Fig. S20†). A comparison of the E_{ad} values of a N_2 molecule at the Ti1 site with different adsorption configurations reveals that the optimal N_2 coordination configuration mentioned above gives the largest E_{ad} value of −3.525 eV, meaning that N_2 activation can be spontaneously realized when it is adsorbed at the Ti1 site. A comparison of the E_{ad} values of N_2 at different sites (Fig. S20†) shows that Ti1 is the strongest active site for N_2 adsorption in r-Ti_3C_2 MXene. In addition, the adjacent Ti1 sites can help to build the optimal coordination configuration for N_2 activation. The more the Ti1 sites are involved, the higher the E_{ad} value is. Moreover, the Ti1 site does not bond with any O atoms. The bond length and adsorption energy of the N_2 molecule at the Ti1 site obtained in our calculations for Ti_3C_2 MXene are very close to those obtained in previous works for Ti_2C MXene.[64,65]

Solar utilization efficiency and stability of r-Ti_3C_2/Au

To evaluate the light utilization efficiency, the wavelength-dependent apparent quantum efficiencies (AQE) of r-T_3C_2/Au were determined by measuring the amount of produced ammonia in pure water under monochromatic light illumination (Fig. 7a). The AQE spectrum of r-Ti_3C_2/Au matches well with its absorption spectrum, suggesting that the ammonia evolution is photo-driven. Specifically, the AQE value for r-Ti_3C_2/Au reaches 0.697% at 520 nm owing to the synergistic effect of the strong plasmonic light harvesting capability of the Au nanospheres and the N_2-activation capability of r-Ti_3C_2. Such an AQE value is higher than those obtained in many previous works at

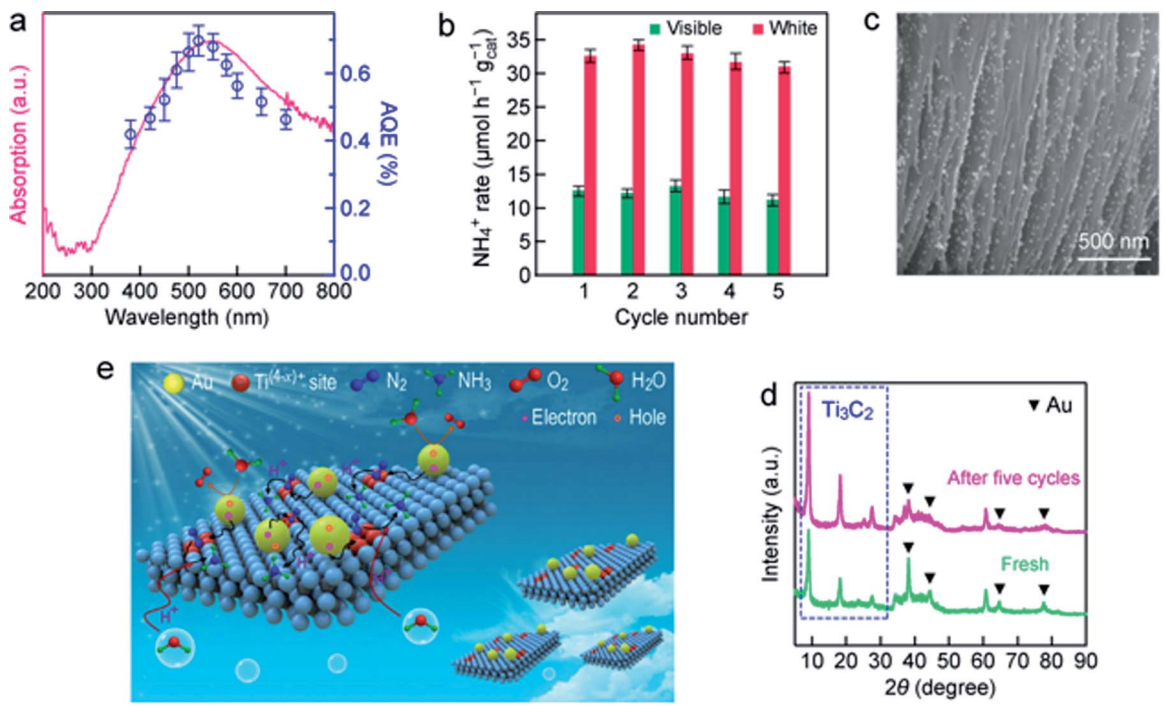

Fig. 7 AQEs and recyclability of r-Ti_3C_2/Au for N_2 photofixation. (a) AQE and absorption spectra. (b) Cyclic tests for N_2 photofixation under white and visible light. (c) SEM image of r-Ti_3C_2/Au after the fifth cycle of test. (d) XRD patterns of the fresh sample and those after the fifth cycle of test. (e) Artistic illustration of the proposed mechanism for photocatalytic N_2 fixation with r-Ti_3C_2/Au.

this wavelength (Tables S2 and S3†). In addition, we also examined the N_2 photofixation activity of r-Ti_3C_2/Au under AM 1.5G solar light illumination in a sealed reactor filled with N_2. The NH_3 production rate was 21.26 μmol h^{-1} $g_{cat}{}^{-1}$, and O_2 was also generated at a rate of 16.12 μmol h^{-1} $g_{cat}{}^{-1}$ in this sealed system (Fig. S21†). The molar ratio of the produced NH_3 and O_2 is close to the theoretical stoichiometric ratio. Accordingly, the solar-to-ammonia conversion efficiency (SACE) was calculated to be 0.013%. The stability of r-Ti_3C_2/Au was evaluated by performing successive rounds of reaction under white and visible light illumination (Fig. 7b). Almost ~95% of the original ammonia generation activity was preserved after five successive cycles, indicative of the high stability of r-Ti_3C_2/Au. The unique sandwich-like structure with uniformly distributed Au nanospheres in the interlayers was well maintained in the used r-Ti_3C_2/Au catalyst (Fig. 7c). The slight decrease in the NH_3 production rate during the cycling tests is believed to be caused by the slight aggregation of the loaded Au nanospheres (Fig. 7c). A negligible amount of the leached Au was detected in the fifth cycle reaction solution by ICP-AES. The stability of r-Ti_3C_2/Au was further confirmed by the nearly unchanged XRD spectrum (Fig. 7d). The photocatalytic stability can be ascribed to the fact that electrons are constantly produced and transferred from the Au nanospheres to Ti_3C_2 under light illumination, which can inhibit the oxidation of Ti_3C_2.

Based on the above results, we propose a reaction mechanism for photocatalytic N_2 fixation with r-Ti_3C_2/Au under ambient conditions (Fig. 7e). Benefiting from the good hydrophilicity, the r-Ti_3C_2/Au photocatalyst can be stably and uniformly dispersed in water. r-Ti_3C_2 possesses numerous low-valence $Ti^{(4-x)+}$ sites that are associated with OVs and generated through H_2 thermal reduction. They are active sites for capturing and activating N_2 molecules. Under light illumination, photogenerated hot electrons from the Au nanospheres are injected into r-Ti_3C_2, which subsequently reduce the activated N_2 at the $Ti^{(4-x)+}$ sites. The hot holes remaining on the Au nanospheres are consumed through the oxidation of H_2O to produce O_2. The produced NH_3 is accumulated in the aqueous reaction solution.

Conclusions

We have demonstrated the potential of Ti_3C_2 MXene to photocatalytically fix N_2 in pure water under ambient conditions. Partially reduced layered Ti_3C_2 MXene is synthesized and integrated with Au nanospheres in a uniform sandwich-like structure through a controlled solvent-driven approach. r-Ti_3C_2 exposes abundant low-valence Ti sites, which act as active sites for capturing and activating N_2 molecules. The embedded Au nanospheres donate plasmonic hot electrons to reduce the activated N_2. Importantly, the unique sandwich-like architecture prevents the self-stacking of the Ti_3C_2 layers, which favors the exposure of the active sites for utilization. The abundant $Ti^{(4-x)+}$ active sites and the LSPR effect work in tandem to endow r-Ti_3C_2/Au with a remarkably high N_2 photofixation activity. The design in this work not only broadens the photocatalytic applications of MXene in N_2 fixation as a host material but also opens up an avenue for the surface engineering of MXene with plasmonic nanoparticles to further explore the potential of MXene as a promising photocatalyst.

Data availability

The data that support the findings of this study are available from the corresponding author upon reasonable request.

Author contributions

B. B. C. performed the experiments and wrote the manuscript. Y. Z. G. assisted with the N_2 photofixation experiments. D. H. W. carried out the density functional theory calculations. L. L., B. C. Y. and J. F. W. designed the research work. J. F. W. revised the manuscript. All authors discussed the results and commented on the manuscript.

Conflicts of interest

There are no conflicts to declare.

Acknowledgements

This work was supported by the National Natural Science Foundation of China (51872110), Shanghai Science and Technology Committee (STCSM, 18490740500), and the Research Grants Council of Hong Kong (GRF, 14305819).

Notes and references

1 H. P. Jia and E. A. Quadrelli, *Chem. Soc. Rev.*, 2014, **43**, 547.
2 C. J. M. Van der Ham, M. T. M. Koper and D. G. H. Hetterscheid, *Chem. Soc. Rev.*, 2014, **43**, 5183.
3 Y. M. Liu and T. J. Meyer, *Proc. Natl. Acad. Sci. U. S. A.*, 2019, **116**, 2794.
4 G. F. Chen, X. R. Cao, S. Q. Wu, X. Y. Zeng, L. X. Ding, M. Zhu and H. H. Wang, *J. Am. Chem. Soc.*, 2017, **139**, 9771.
5 A. Klerke, C. H. Christensen, J. K. Nørskov and T. Vegge, *J. Mater. Chem.*, 2008, **18**, 2304.
6 S. Licht, B. C. Cui, B. H. Wang, F. F. Li, J. Lau and S. Z. Liu, *Science*, 2014, **345**, 637.
7 D. Bao, Q. Zhang, F. L. Meng, H. X. Zhong, M. M. Shi, Y. Zhang, J. M. Yan, Q. Jiang and X. B. Zhang, *Adv. Mater.*, 2017, **29**, 1604799.
8 H. Li, C. L. Mao, H. Shang, Z. P. Yang, Z. H. Ai and L. Z. Zhang, *Nanoscale*, 2018, **10**, 15429.
9 H. Li, J. Shang, Z. H. Ai and L. Z. Zhang, *J. Am. Chem. Soc.*, 2015, **137**, 6393.
10 W. K. Wang, H. M. Zhang, S. B. Zhang, Y. Y. Liu, G. Z. Wang, C. H. Sun and H. J. Zhao, *Angew. Chem., Int. Ed.*, 2019, **58**, 16644.
11 H. Hirakawa, M. Hashimoto, Y. Shiraishi and T. Hirai, *J. Am. Chem. Soc.*, 2017, **139**, 10929.
12 G. N. Schrauzer and T. D. Guth, *J. Am. Chem. Soc.*, 1977, **99**, 7189.

13 C. M. Janet, S. Navaladian, B. Viswanathan, T. K. Varadarajan and R. P. Viswanath, *J. Phys. Chem. C*, 2010, **114**, 2622.
14 X. L. Xue, R. P. Chen, H. W. Chen, Y. Hu, Q. Q. Ding, Z. T. Liu, L. B. Ma, G. Y. Zhu, W. J. Zhang, Q. Yu, J. Liu, J. Ma and Z. Jin, *Nano Lett.*, 2018, **18**, 7372.
15 C. K. Yao, R. Wang, Z. S. Wang, H. Lei, X. P. Dong and C. Z. He, *J. Mater. Chem. A*, 2019, **7**, 27547.
16 Q. X. Liu, L. H. Ai and J. Jiang, *J. Mater. Chem. A*, 2018, **6**, 4102.
17 Y. C. Hao, X. L. Dong, S. R. Zhai, H. C. Ma, X. Y. Wang and X. F. Zhang, *Chem.–Eur. J.*, 2016, **22**, 18722.
18 H. L. Jia, A. Du, H. Zhang, J. H. Yang, R. B. Jiang, J. F. Wang and C. Y. Zhang, *J. Am. Chem. Soc.*, 2019, **141**, 5083.
19 H. Diarmand-Khalilabad, A. Habibi-Yangjeh, D. Seifzadeh, S. Asadzadeh-Khaneghah and E. Vesali-Kermani, *Ceram. Int.*, 2019, **45**, 2542.
20 Y. F. Sun, S. Gao, F. C. Lei and Y. Xie, *Chem. Soc. Rev.*, 2015, **44**, 623.
21 Y. F. Sun, S. Gao, F. C. Lei, C. Xiao and Y. Xie, *Acc. Chem. Res.*, 2015, **48**, 3.
22 Q. Su, Y. Li, R. Hu, F. Song, S. Y. Liu, C. P. Guo, S. M. Zhu, W. B. Liu and J. Pan, *Adv. Sustainable Syst.*, 2020, **4**, 2000130.
23 M. Naguib, M. Kurtoglu, V. Presser, J. Lu, J. J. Niu, M. Heon, L. Hultman, Y. Gogotsi and M. W. Barsoum, *Adv. Mater.*, 2011, **23**, 4248.
24 M. Naguib, V. N. Mochalin, M. W. Barsoum and Y. Gogotsi, *Adv. Mater.*, 2014, **26**, 992.
25 B. Anasori, M. R. Lukatskaya and Y. Gogotsi, *Nat. Rev. Mater.*, 2017, **2**, 16098.
26 X. B. Hui, X. L. Ge, R. Z. Zhao, Z. Q. Li and L. W. Yin, *Adv. Funct. Mater.*, 2020, **30**, 2005190.
27 Z. Li and Y. Wu, *Small*, 2019, **15**, 1804736.
28 J. H. Peng, X. Z. Chen, W. J. Ong, X. J. Zhao and N. Li, *Chem*, 2019, **5**, 18.
29 R. D. Tang, S. Xiong, D. X. Gong, Y. C. Deng, Y. C. Wang, L. Su, C. X. Ding, L. H. Yang and C. J. Liao, *ACS Appl. Mater. Interfaces*, 2020, **12**, 56663.
30 X. Li, Y. Bai, X. Shi, N. Su, G. Z. Nie, R. M. Zhang, H. B. Nie and L. Q. Ye, *Mater. Adv.*, 2021, **2**, 1570.
31 L. M. Azofra, N. Li, D. R. Macfarlane and C. H. Sun, *Energy Environ. Sci.*, 2016, **9**, 2545.
32 K. L. Huang, C. H. Li, H. Z. Li, G. M. Ren, L. Wang, W. T. Wang and X. C. Meng, *ACS Appl. Nano Mater.*, 2020, **3**, 9581.
33 L. F. Hong, R. T. Guo, Y. Yuan, X. Y. Ji, Z. S. Li, Z. D. Lin and W. G. Pan, *Mater. Today Energy*, 2020, **18**, 100521.
34 J. Z. Qin, X. Hu, X. Y. Li, Z. F. Yin, B. J. Liu and K. H. Lam, *Nano Energy*, 2019, **61**, 27.
35 J. H. Yang, Y. Z. Guo, W. Z. Lu, R. B. Jiang and J. F. Wang, *Adv. Mater.*, 2018, **30**, 1802227.
36 J. H. Yang, Y. Z. Guo, R. B. Jiang, F. Qin, H. Zhang, W. Z. Lu, J. F. Wang and J. C. Yu, *J. Am. Chem. Soc.*, 2018, **140**, 8497.
37 C. Y. Hu, X. Chen, J. B. Jin, Y. Han, S. M. Chen, H. X. Ju, J. Cai, Y. R. Qiu, C. Gao, C. M. Wang, Z. M. Qi, R. Long, L. Song, Z. Liu and Y. J. Xiong, *J. Am. Chem. Soc.*, 2019, **141**, 7807.
38 T. T. Hou, L. L. Chen, Y. Xin, W. K. Zhu, C. Y. Zhang, W. H. Zhang, S. Q. Liang and L. B. Wang, *ACS Energy Lett.*, 2020, **5**, 2444.
39 P. Zhang, T. Wang and J. L. Gong, *Adv. Mater.*, 2015, **27**, 5328.
40 J. H. Yang, H. Y. Bai, Y. Z. Guo, H. Zhang, R. B. Jiang, B. C. Yang, J. F. Wang and J. C. Yu, *Angew. Chem., Int. Ed.*, 2021, **60**, 927.
41 T. B. Limbu, B. Chitara, J. D. Orlando, M. Y. Garcia Cervantes, S. Kumari, Q. Li, Y. Tang and F. Yan, *J. Mater. Chem. C*, 2020, **8**, 4722.
42 Y. Y. Wen, T. E. Rufford, X. Z. Chen, N. Li, M. Q. Lyu, L. M. Dai and L. Z. Wang, *Nano Energy*, 2017, **38**, 368.
43 M. Ghidiu, S. Kota, J. Halim, A. W. Sherwood, N. Nedfors, J. Rosen, V. N. Mochalin and M. W. Barsoum, *Chem. Mater.*, 2017, **29**, 1099.
44 C. J. Zhao, Q. Wang, H. Zhang, S. Passerini and X. Z. Qian, *ACS Appl. Mater. Interfaces*, 2016, **8**, 15661.
45 G. D. Zou, Z. W. Zhang, J. X. Guo, B. Z. Liu, Q. R. Zhang, C. Fernandez and Q. M. Peng, *ACS Appl. Mater. Interfaces*, 2016, **8**, 22280.
46 J. X. Low, L. Y. Zhang, T. Tong, B. J. Shen and J. G. Yu, *J. Catal.*, 2018, **361**, 255.
47 A. A. Khan, M. Tahir and A. Bafaqeer, *Energy Fuels*, 2020, **34**, 9810.
48 R. B. Rakhi, B. Ahmed, M. N. Hedhili, D. H. Anjum and H. N. Alshareef, *Chem. Mater.*, 2015, **27**, 5314.
49 X. L. Li, X. W. Yin, M. K. Han, C. Q. Song, H. L. Xu, Z. X. Hou, L. T. Zhang and L. F. Cheng, *J. Mater. Chem. C*, 2017, **5**, 4068.
50 Y. Yoon, T. A. Le, A. P. Tiwari, I. Kim, M. W. Barsoum and H. Lee, *Nanoscale*, 2018, **10**, 22429.
51 H. Wang, Y. Wu, X. Z. Yuan, G. Zeng, J. Zhou, X. Wang and J. W. Chew, *Adv. Mater.*, 2018, **30**, 1704561.
52 R. Y. Li, L. B. Zhang, L. Shi and P. Wang, *ACS Nano*, 2017, **11**, 3752.
53 Y. Z. Guo, J. H. Yang, D. H. Wu, H. Y. Bai, Z. Yang, J. F. Wang and B. C. Yang, *J. Mater. Chem. A*, 2020, **8**, 16218.
54 S. Y. Moon, H. C. Song, E. H. Gwag, L. I. Nedrygailov, C. Lee, J. J. Kim, W. H. Doh and J. Y. Park, *Nanoscale*, 2018, **10**, 22180.
55 S. Y. Wang, X. Hai, X. Ding, K. Chang, Y. G. Xiang, X. G. Meng, Z. X. Yang, H. Chen and J. H. Ye, *Adv. Mater.*, 2017, **29**, 1701774.
56 J. Liu, M. S. Kelley, W. Q. Wu, A. Banerjee, A. P. Douvalis, J. S. Wu, Y. B. Zhang, G. C. Schatz and M. G. Kanatzidis, *Proc. Natl. Acad. Sci. U. S. A.*, 2016, **113**, 5530.
57 Y. X. Zhao, Y. F. Zhao, R. Shi, B. Wang, G. I. N. Waterhouse, L. Z. Wu, C. H. Tung and T. R. Zhang, *Adv. Mater.*, 2019, **31**, 1806482.
58 D. Liu, G. Zhang, Q. H. Ji, Y. Y. Zhang and J. H. Li, *ACS Appl. Mater. Interfaces*, 2019, **11**, 25758.
59 C. D. Lv, Y. M. Qian, C. S. Yan, Y. Ding, Y. Y. Liu, G. Chen and G. H. Yu, *Angew. Chem., Int. Ed.*, 2018, **57**, 10246.
60 X. M. Li, X. Sun, L. Zhang, S. M. Sun and W. Z. Wang, *J. Mater. Chem. A*, 2018, **6**, 3005.
61 L. R. Johnson, S. Sridhar, L. Zhang, K. D. Fredrickson, A. S. Raman, J. Jang, C. Leach, A. Padmanabhan,

C. C. Price, N. C. Frey, A. Raizada, V. Rajaraman, S. Saiprasad, X. Tang and A. Vojvodic, *ACS Catal.*, 2020, **10**, 253.

62 Y. Tanabe and Y. Nishibayashi, *Coord. Chem. Rev.*, 2013, **257**, 2551.

63 M. A. Legare, G. Belanger-Chabot, R. D. Dewhurst, E. Welz, I. Krummenacher, B. Engels and H. Braunschweig, *Science*, 2018, **359**, 896.

64 J. D. Gouveia, Á. Morales-García, F. Viñes, J. R. B. Gomes and F. Illas, *ACS Catal.*, 2020, **10**, 5049.

65 S. Li, G. Liu, Z. Liu, W. Hu and H. Deng, *J. Mater. Chem. A*, 2019, **7**, 19950.